Phonon-blocked junction calorimeter

Zhuoran Geng,[1, *] Joel Hätinen,[2] Emma Mykkänen,[2] Mika Prunnila,[2, †] and Ilari J. Maasilta[1, ‡]

[1]*Nanoscience Center, Department of Physics, University of Jyväskylä,*
P. O. Box 35, FIN-40014 Jyväskylä, Finland
[2]*VTT Technical Research Center of Finland Ltd.,*
P. O. Box 1000, FIN-02044 VTT Espoo, Finland
(Dated: August 8, 2025)

This study introduces a cold-electron microcalorimeter based on phonon-blocked junctions, integrating on-chip electron cooling and boundary phonon isolation to achieve exceptional energy resolution and rapid thermal response. A general theoretical framework is presented, along with derived approximate analytical expressions for key performance metrics, including cooling efficiency, thermal time constant, and energy resolution. The work examines the influence of device parameters, including non-ideal effects such as subgap tunneling and heat backflow, and offers insights into optimizing detector performance. The findings highlight the potential of phonon-blocked junction microcalorimeters to rival or outperform the state-of-art technologies, such as transition-edge sensors, paving the way for applications requiring precise and fast energy detection.

arXiv:2508.05490v1 [physics.ins-det] 7 Aug 2025

I. INTRODUCTION

Over the past two decades, cryogenic microcalorimeters have emerged as critical tools in fields as diverse as particle physics, astrophysics, material science, and life sciences[1, 2]. These detectors rely on ultra-sensitive thermometers, operating at low temperatures, to capture temperature changes caused by the energy transfer of particles in an absorber. The performance of these devices is typically measured by their energy resolution, ΔE, which quantifies how precisely they can measure the energy of individual particles. For non-dispersive sensors, the energy resolution is inherently limited by thermodynamic fluctuation noise (TFN), caused by random phonon exchanges between the absorber and the heat sink. In a system where the absorber has a thermal capacity C_{th} and operates at a bath temperature T_B provided by the external refrigeration, the full-width half-maximum (FWHM) energy resolution is given by $\Delta E_{\mathrm{intrinsic}} = 2.35\sqrt{k_B T_B^2 C_{\mathrm{th}}}$ [1, 3, 4]. The practical energy resolution of most cryogenic microcalorimeters is often expressed as $\Delta E = \xi \Delta E_{\mathrm{intrinsic}}$, where the normalized resolution ξ reflects the detector's sensitivity and noise characteristics[1].

Among X-ray detectors, the transition-edge sensor (TES) has emerged as one of the most sensitive microcalorimeter technologies available today[5, 6]. TES uses electro-thermal feedback to improve energy resolution, achieving a factor of $\xi = 2.4/\sqrt{\alpha_{\mathrm{TES}}}$[1, 7], where α_{TES}, a measure of sensitivity, can exceed 100. Such sensitivity, many orders of magnitude better than that of conventional solid-state detectors, sets a new benchmark in X-ray detection. However, TES technology is not

without its challenges. Optimizing the resolution often requires fabricating TES devices on fragile membranes to control phonon flow between the sensor and thermal bath, which complicates fabrication and reduces mechanical stability as well as significantly increases the thermal recovery time. Additionally, TES detectors require sophisticated external refrigeration, often cooling to below 100 mK, to achieve optimal resolution and offset the additional Joule heating from electro-thermal feedback, which can be significant in large arrays.

In this study, we present a general theory on the cold-electron microcalorimeter based on phonon-blocked tunnel junctions[8]. In this design, the radiation absorber is thermally linked to the bath via phonon-blocked junctions, which simultaneously operate as the electro-thermal sensing and cooling elements, and barriers to phonon heat transport. The junctions employed in this device is a pair of normal metal-insulator-superconductor (NIS) junctions, where the normal metal serves as both the radiation absorber and the metallic electrode. NIS devices, known for their use in on-chip cooling and precise thermometry in the sub-kelvin temperature range[9, 10], exploit the gap in the density of states (DOS) of the superconductor electrode as an energy filter for electrons. The phonon-blocked architecture minimizes phononic thermal conduction, thereby enhancing thermal isolation and improving the effectiveness of the electron cooling.

Historically, cold-electron microbolometers based on NIS junctions have been regarded as promising cryogenic detectors and have been extensively studied, both theoretically[11–15] and experimentally[16, 17]. In contrast, research on NIS junction-based microcalorimeters has been relatively limited[18, 19], and they have generally been considered less effective compared to TES technology[20]. However, our findings suggest otherwise.

By optimizing the interface property of the junction and considering the self-cooling effect of the absorber, we demonstrate that an optimized NIS calorimeter can

---

* zhgeng@jyu.fi
† mika.prunnila@vtt.fi
‡ maasilta@jyu.fi

achieve a normalized energy resolution of $\xi = 3.3(1 - \eta)$, where η represents a relative cooling factor and has been reported to reach up to 80% experimentally[17]. These results indicate that the phonon-blocked microcalorimeter could rival or even outperform TES in energy resolution and speed, setting a new benchmark for cryogenic microcalorimetry.
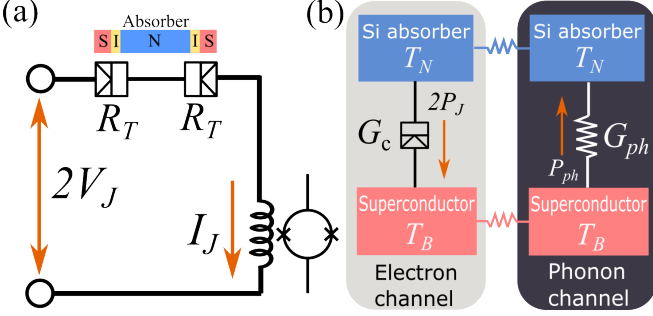
II.   DETECTOR MODEL

FIG. 1. (a) Schematic of the the electric circuit of the system, consisting a pair of NIS junctions and readout circuit. (b) Thermal model of the system, illustrating the heat flows in the electron and phonon channels.

To detect particle energy, a calorimetric device typically comprises several key components, each designed to fulfill specific functions[6]. These include an absorber to capture the incident photon and convert its energy to heat; a sensing element to transduce this thermal excitation into a measurable electrical signal; and thermal impedance to control heat flow between the sensor and the bath, ensuring proper thermal isolation.

In our model, a large normal metal electrode functions as the absorber, while two identical NIS tunnel junctions, acting as the temperature sensors, are created by adding superconducting contacts to the common normal metal electrode, separated by thin insulating barriers. Figure 1(a) presents the general electrical model of the device, where each NIS junction has a tunnel resistance of R_T, and is biased with a constant voltage V_J. The resulting current signal, I_J, is read by a superconducting quantum interference device (SQUID) through an input coil connected in series with the tunnel junctions.

Heat flow between the sensor and the bath occurs through both electron and phonon channels, as illustrated in Fig. 1(b). A crucial aspect of our model is that the phonon-blocked junction provides thermal isolation in the phonon channel[8, 21, 22]. Phonon heat leakage is limited by interfacial thermal resistances[23], governed by the equation:

$$P_{\text{ph}} = \frac{1}{4a_{\text{eITR}}}(T_B^4 - T_N^4) \tag{1}$$

where a_{eITR} is the effective interfacial thermal resistance coefficient, T_B and T_N represent the phonon temperature

of the bath and absorber, respectively. In our model, we assume the temperature of the superconducting electrode equilibrates with that of the thermal bath T_B. This simplification is justified by two considerations: first, in the large-volume of the superconductor electrode, the electron–phonon coupling is sufficiently strong to ensure that electrons and phonons remain in equilibrium. Secondly, the large contact area between the electrode and the substrate minimizes any interfacial thermal resistance. Together, these factors allow us to treat the electrode and bath as sharing a common temperature. Likewise, both the electron and phonon systems in the absorber are assumed to be at the same temperature T_N, which is justified by the strong electron-phonon coupling in the large-volume normal metal. Consequently, the heat currents in the electron and phonon channels are simplified to $2P_J$, the cooling power generated by the tunnel junctions, and P_{ph}, the heat current associated with the phonon flow, respectively.

When a small incident power P_{in} is absorbed by the detector, the temperature T_N rises in accordance with the heat balance equation derived from the thermal model in Fig.1(b):

$$C_{\text{th}}\frac{\mathrm{d}}{\mathrm{d}t}T_N + 2P_J - P_{\text{ph}} = P_{\text{in}} + 2\beta(P_J + I_J V_J). \tag{2}$$

In this expression, the heat capacity $C_{\text{th}} = \gamma T_N$ of the absorber is assumed to be dominated by the electron system at the relevant temperature, with γ is the Sommerfeld coefficent multiplied by absorber volume. The factor 2β accounts for the portion of heat dissipated by quasiparticles in the superconductor that returns to the absorber via the pair of junctions, adding to the signal and phonon transport heat[24]. Due to the low resistance of the normal metal, direct Joule heating is negligible [25].

The electric current I_J and cooling power $2P_J$ generated by the pair of NIS junctions are given by[26, 27]:

$$I_J(V_J, T_N, T_B) = \frac{1}{eR_T}\int_{-\infty}^{\infty} \mathrm{d}\epsilon\, N_S(\epsilon, T_B)$$
$$\times \left[f(\epsilon + eV_J, T_N) - f(\epsilon, T_B)\right], \tag{3}$$

$$P_J(V_J, T_N, T_B) = \frac{1}{e^2 R_T}\int_{-\infty}^{\infty} \mathrm{d}\epsilon\, (\epsilon + eV_J)N_S(\epsilon, T_B)$$
$$\times \left[f(\epsilon + eV_J, T_N) - f(\epsilon, T_B)\right]. \tag{4}$$

Here $f(\epsilon, T)$ is the Fermi-Dirac distribution, and $N_S(\epsilon, T_B)$ is the superconductor density of states:

$$N_S(\epsilon, T_B) = \left|\text{Re}\left[\frac{\epsilon/\Delta_0 + i\Gamma}{\sqrt{(\epsilon/\Delta_0 + i\Gamma)^2 - \Delta^2(T_B)/\Delta_0^2}}\right]\right|,$$

where $\Delta(T_B)$ and Δ_0 represent the superconducting gap at temperature T_B and zero temperature limit, and Γ is the dimensionless Dynes parameter that characterizes subgap tunneling behavior[28].

At low temperatures ($k_B T \ll \Delta_0$), the optimal bias voltage V_{opt} at each junction for maximizing cooling
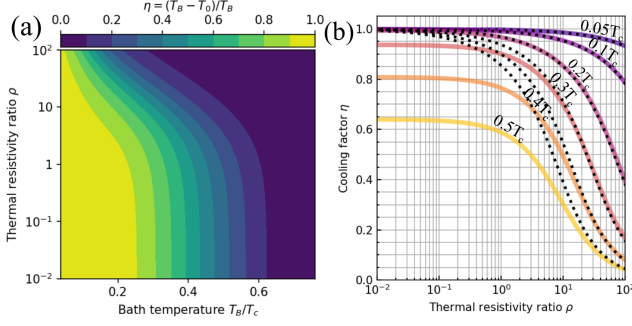
FIG. 2. (a) The relative cooling factor η as a function of the normalized bath temperature T_B/T_c, and resistivity ratio ρ. (b) Comparison of η between the numerical (colored solid lines) and the analytical solution (black dotted lines) as a function of ρ.

power P_J can be approximated by $eV_{\mathrm{opt}} = \Delta_0 - 0.66k_BT_N$[9, 10, 14]. Under this optimal bias, the junction current and cooling power simplify to[8]:

$$I_J(V_{\mathrm{opt}}) \approx 0.48\frac{\sqrt{k_BT_N\Delta_0}}{eR_T}, \tag{5}$$

$$P_J(V_{\mathrm{opt}}) \approx \frac{\Delta_0^2}{e^2R_T}\left[0.59\left(\frac{k_BT_N}{\Delta_0}\right)^{\frac{3}{2}} - \sqrt{\frac{2\pi}{\beta_B}}e^{-\beta_B}\right]$$
$$- \frac{V_{\mathrm{opt}}^2}{2R_T}\Gamma, \tag{6}$$

where $\beta_B = \Delta_0/k_BT_B$ is introduced for clarity. In addition, the heat current ratio flowing between the two channels can also be approximated by $P_{\mathrm{ph}}/P_J \approx 0.42\rho[(T_B/T_N)^4 - (T_N/T_c)^{2.5}]$ in the low-temperature limit, where

$$\rho = \frac{R_T}{a_{\mathrm{eITR}}}\frac{e^2T_c^2}{k_B^2\sqrt{\Delta_0/k_BT_c}} \tag{7}$$

is a dimensionless parameter characterizing the resistivity ratio between the electron and phonon channels, and it describes the interface property of the tunnel junction independent to the area size.

In the quiescent state, where $P_{\mathrm{in}} = 0$, the heat balance becomes $2P_J(V_b, T_N, T_B) = P_{\mathrm{ph}}(T_N, T_B)$, assuming ideal detector parameters with $\Gamma = 0$ and $\beta = 0$. At such state, the absorber reaches an equilibrium temperature T_0, which can be approximated by solving:

$$\left(\frac{T_B}{T_c}\right)^4 - \left(\frac{T_0}{T_c}\right)^4 = \frac{4.72}{\rho}\left(\frac{T_0}{T_c}\right)^{1.5}. \tag{8}$$

To provide a dimensionless measure of cooling performance, here we introduce a relative cooling factor defined as[8]

$$\eta = \frac{T_B - T_0}{T_B}. \tag{9}$$

As shown in Fig. 2(a), η increases as both the bath temperature T_B and the resistivity ratio ρ decreases. One notable feature is that η approaches a limiting value at low ρ ($\rho < 1$), which is shown more clear on panel (b) in which η is plotted as a function of ρ for different bath temperature (colored solid lines). Panel (b) also compares numerical results (colored solid lines) with the analytical approximation from Eq. (8) (black dotted lines), showing excellent agreements for bath temperature below $0.3T_c$.

III. CALORIMETRIC RESPONSE

When a photon is stopped by the detector, its energy is instantly converted into energetic excitations within a small volume of the absorber. These excitations undergo diffusion and scattering, gradually distributing their energy as heat, forming a thermal equilibrium over time. The thermal diffusion time of the charge carriers within the metal absorber is typically on the order less than microseconds, which is much shorter than the thermal time constant τ_{th}, the time it takes for heat to transfer from the absorber to the thermal bath. Due to this disparity in timescales, we can approximate that the absorber experiences an initial temperature rise, given by $\Delta T = E/C_{\mathrm{th}}$[29], where E is the photon's energy and C_{th} is the absorber's heat capacity. This rapid temperature rise, followed by its gradual evolution, is measured by a temperature-sensitive element, which in this case are the NIS tunnel junctions. By tracking the current signal $I_J(t)$ over time, the photon's energy can be accurately determined.

The detector's responsivity S_I, which defines the power-to-current transfer function, plays a key role in characterizing the conversion between the input heat and the measurable electrical signal. When the input power variation ΔP_{in} is small, the responsivity $S_I = \Delta I_J/\Delta P_{\mathrm{in}}$ can be approximated using a first-order linearization based on the thermal and electrical balance equations of the detector. To express this relationship, we define T_0, I_0, and V_0 as the absorber temperature, junction current, and junction voltage in the quiescent state, respectively. The small deviations in the variables, $\Delta T_N = T_N - T_0$, $\Delta I_J = I_J - I_0$, and $\Delta V_J = V_J - V_0$, can then be written as:

$$\Delta P_{\mathrm{in}} = (1 + i\omega\tau_{\mathrm{th}})G_{\mathrm{th}}\Delta T_N - (2R_NI_0 + 2\beta V_0)\Delta I_J$$
$$+ \frac{V_0}{R_J}b_0\Delta V_J + \delta P,$$
$$\Delta I_J = \alpha_T\frac{I_0}{T_0}\Delta T_N + \frac{1}{R_J}\Delta V_J + \delta I,$$
$$\Delta V_J = -(R_N + i\omega L)\Delta I_J + \delta V. \tag{10}$$

Here the equations are expressed in the frequency domain, with ω representing the angular frequency of the detector's signal. The terms δP, δI, and δV refer to small perturbations from intrinsic fluctuations.

The linearized coefficients appearing in Eqs.(10) are critical for understanding the detector's thermal and electrical response. These coefficients include the thermal conductance in the phonon channel, $G_{\text{ph}} = T_0^3/a_{\text{eITR}}$, and the total dynamic thermal conductance in electron channel, $G_c = 2\partial P_J/\partial T$. The junction dynamic resistance is defined as $R_J = \partial V_J/\partial I_J$, while the junction's dimensionless sensitivities to temperature and voltage are given by $\alpha_T = \partial \ln I_J/\partial \ln T_N$ and $\alpha_V = \partial \ln P_J/\partial \ln V_J$, respectively.

In addition to these, we define $G_{\text{th}} = G_{\text{ph}}+(1-\beta)G_c$ as the total thermal conductance including the fraction from the backflow, $\tau_{\text{th}} = C_{\text{th}}/G_{\text{th}}$ as the thermal time constant of the system, and $b_0 = 2\left[\alpha_V - \beta(\alpha_V + I_0V_0/P_0)\right] \cdot \left(P_0R_J/V_0^2\right)$ as a constant which simplifies calculations of the current response[30].

Equations (10) demonstrate the interconnected nature of the thermal and electrical behavior of the detector through state variables ΔP, ΔI, and ΔV. In an optimal case where $\beta = 0$, the equations simplify to $\Delta P_{\text{in}} = (1+i\omega\tau_{\text{th}})G_{\text{th}}\Delta T_N+\delta P$ and $\Delta I_J = (\alpha_T I_0/T_0)\Delta T_N+\delta I$, eliminating feedback from the output signal to the temperature change and simplifying the analysis.

With this simplification, the frequency-dependent responsivity can be derived as:

$$S_I(\omega) = \frac{\mathcal{L}_0}{(1 + i\omega\tau_{\text{th}})V_J}, \quad (11)$$

where $\mathcal{L}_0 = \alpha_T I_0 V_J/G_{\text{th}}T_0$ represents a dimensionless factor analogous to the zero-frequency loop gain commonly used in calorimetric analysis[1, 9].
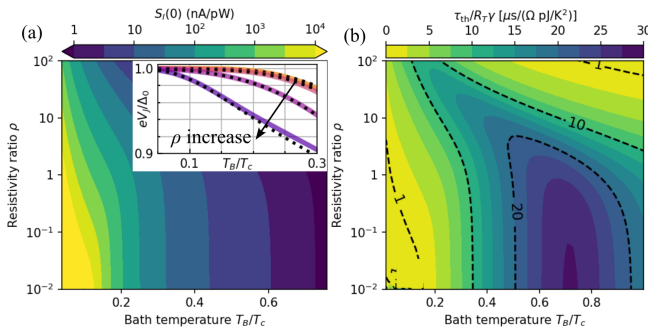

FIG. 3. (a) Zero-frequency responsivity $S_I(0)$ as a function of the normalized bath temperature T_B/T_c and resistivity ratio ρ. The inset compares the bias voltage maximizing $S_I(0)$ with approximate V_{opt} at different ρ. (b) The thermal time constant τ, scaled by γR_T, as a function of T_B/T_c and ρ.

Equation (11) indicates that the responsivity has a cutoff frequency at $\omega_0 = \tau_{\text{th}}^{-1}$ and remaining constant at low frequency. Figure 3(a) illustrates the numerical results for zero-frequency responsivity $S_I(0)$ as a function of bath temperature and resistivity ratio of ρ in an ideal device, showing that decreasing T_B and ρ increases $S_I(0)$. The bias voltage that maximizes responsivity is plotted in the inset of panel (a) as function of T_B/T_c by the colored solid lines which align closely with the approximate

optimal bias V_{opt}, represented by the black dotted line, at $T_B < 0.2T_c$.

This alignment allows us to derive an approximate expression for optimal S_I. At V_{opt}, the total thermal conductance is given by $G_{\text{th}} \approx T_0^3/a_{\text{eITR}} + 1.77k_B\sqrt{k_BT_0\Delta_0}/e^2R_T$, while the temperature sensitivity is approximately $\alpha_T \approx 1$. Consequently, the low-frequency responsivity can be approximated as:

$$S_I(0) \approx 0.48\frac{e}{k_BT_c}\left[1.77\frac{T_0}{T_c} + \frac{1}{\rho}\left(\frac{T_0}{T_c}\right)^{3.5}\right]^{-1}. \quad (12)$$

In this expression, the second term diminishes rapidly with decreasing temperature, simplifying to approximately $3.15/T_0$ (nA/pW) in the low-temperature limit, only inversely proportional to the electron temperature of the absorber and independent to its volume. This result is lower than that reported in previous research[13] by a factor of two, owing to a double junction configuration used in this study.

The thermal time constant, τ_{th}, characterizes the evolution of the absorber's temperature over time, following the expression $T_N(t) = (E/C_{\text{th}})\exp(-t/\tau_{\text{th}})$ for calorimeters without feedback[18]. At the optimal bias, τ_{th} can be approximated at quiescent temperature T_0 as:

$$\tau_{\text{th}} \approx \gamma\left(\frac{T_0^2}{a_{\text{eITR}}} + 1.77\frac{k_B^2}{e^2R_T}\sqrt{\frac{\Delta_0}{k_BT_0}}\right)^{-1}. \quad (13)$$

This expression indicates that τ_{th} decreases at both high and low temperatures, while increasing within an intermediate range, creating a pivot point at $T_0/T_c = (0.44/\rho)^{0.4}$. Figure 3(b) illustrates the thermal time, scaled to $\tau_{\text{th}}/\gamma R_T$, showing a clear bell-shaped distribution as a function of bath temperature, with lower values at both extremes. In the low-temperature limit, the thermal time constant is primarily governed by the electrical channel, following $\tau_{\text{th}} \propto \gamma R_T\sqrt{T_0}$. This suggests that operating at lower temperatures enhances both the sensitivity and the speed of the detector. This behavior is a notable characteristic that sets the cold-electron microcalorimeter apart from other conventional cryogenic microcalorimeters. In contrast, a TES detector exhibits a valley-shaped dependence on bath temperature, which limits its speed at lower temperatures[1]. For example, in the device presented with $C_{\text{th}} = 0.8$ pJ/K at 0.1 K, the thermal time constant is $\tau_{\text{th}}/R_T < 50$ μs/Ω when ρ is low, significantly outperforming state-of-the-art TES devices with similar heat capacities[5, 31–34].

Additionally, it is worth noting that for an ideal detector, the zero-frequency responsivity $S_I(0)$ governed by the resistivity ratio ρ, is independent of the tunnel junction's dimensions. In contrast, the detector speed, is determined by the thermal time constant scales with the junction area. Notably, in the low-temperature limit, Eq.(12) reduces to its first term, eliminating explicit dependence on R_T. This suggests that for applications requiring high signal bandwidth, using large-area tunnel

junctions is beneficial, as they can increase bandwidth without compromising responsivity.

IV. NOISE AND ENERGY RESOLUTION

The energy resolution, ΔE, is the key measure of a microcalorimeter's performance in detecting the energy of individual particles. While the introduction addressed that the intrinsic resolution is limited by thermodynamic fluctuation noise (TFN), as expressed by $\Delta E_{\text{intrinsic}} = 2.35\sqrt{k_B T_B^2 C_{\text{th}}}$, additional noise sources must be considered in practical applications for accurate performance analysis. One major contributor is shot noise, which arises from the fluctuations in the number of electrons passing through the voltage-biased tunnel junction, generating noise in both electrical and heat currents[13, 14, 35]. Furthermore, amplifier noise from the readout electronics and Johnson noise from the absorber's resistance also contribute to the overall noise budget. As a result, only signal power exceeding the combined noise power from all these sources will carry useful information about the absorbed particle.

To accurately account for these various noise sources, the minimal measurable energy ΔE can be estimated by examining the total noise power spectral density in the frequency domain. For stationary noise, the measurement in each frequency interval, $d\omega$, is statistically independent of others, and the FWHM energy resolution is given by[29]:

$$\Delta E = 2.35\left[\int_0^\infty \frac{2}{\pi}\frac{1}{\text{NEP}_{\text{tot}}^2(\omega)}d\omega\right]^{-\frac{1}{2}}, \qquad (14)$$

where $\text{NEP}_{\text{tot}}(\omega)$ represents the total noise equivalent power, which defines the signal power required in a 1-Hz bandwidth to match the noise.

The total NEP is derived by summing all contributing noise sources:

$$\text{NEP}_{\text{tot}}^2 = \text{NEP}_{\text{TFN}}^2 + 2\text{NEP}_{\text{Junc}}^2 + \text{NEP}_{\text{Amp}}^2 + \text{NEP}_{\text{John}}^2, \qquad (15)$$

where each term represents a specific source of noise. These contributions can be evaluated from the small power variation, $\langle\Delta P^2\rangle$, induced by the fluctuations applied to the perturbation terms in Eqs.(10). Specifically, NEP_{TFN} corresponds to thermodynamic power fluctuations, δP_{TFN}; NEP_{Junc} arises from shot noise at each junction, incorporating both power fluctuations, δP_J, and current fluctuations, δI_J; NEP_{Amp} stems from readout noise due to current fluctuations, δI_{Amp}; and NEP_{John}, which represents voltage fluctuations, δV_{John}, generated by the resistance of the absorber and is considered negligible compared to other sources in this study.

As a result, the total NEP can be expressed as:

$$\text{NEP}_{\text{tot}}^2(\omega) = \langle\delta P_{\text{TFN}}^2\rangle + \frac{\langle\delta I_{\text{Amp}}^2\rangle}{|S_I(\omega)|^2}$$
$$+ 2\left[\langle\delta P_J^2\rangle + \frac{\langle\delta I_J^2\rangle}{|S_I(\omega)|^2} + 2\text{Re}\left(\frac{1}{S_I(\omega)}\right)\langle\delta I_J\delta P_J\rangle\right], \qquad (16)$$

where we assume no correlations between TFN, junction noise, and Johnson noise, but allow for cross-correlation between the junction electrical and heat current fluctuations. It is also worth-noting that the cross-correlation term $\langle\delta I_J\delta P_J\rangle$ is generally negative valued, leading to a reduction in the total NEP.

At quiescent temperature T_0, the expected contribution from thermodynamic fluctuation noise (TFN) is expressed as[14]:

$$\langle\delta P_{\text{TFN}}^2\rangle = 2\frac{\zeta(5)}{\zeta(4)}\frac{k_B}{a_{\text{eITR}}}(T_0^5 + T_B^5)$$
$$\approx 1.92\frac{k_B}{a_{\text{eITR}}}(T_0^5 + T_B^5) \qquad (17)$$

The junction's noise spectral density components, which include both current and power fluctuations as well as their cross-correlation, are given in[13] as follows:

$$\langle\delta I_J^2\rangle = \frac{2}{R_T}\int_{-\infty}^\infty d\epsilon\, N_S(\epsilon, T_B)(f_N + f_S - 2f_N f_S),$$
$$\langle\delta P_J^2\rangle = \frac{2}{e^2 R_T}\int_{-\infty}^\infty d\epsilon\, (\epsilon + eV_J)^2 N_S(\epsilon, T_B)$$
$$\times (f_N + f_S - 2f_N f_S),$$
$$\langle\delta I_J\delta P_J\rangle = \frac{2}{eR_T}\int_{-\infty}^\infty d\epsilon\, (\epsilon + eV_J)N_S(\epsilon, T_B)$$
$$\times (f_N + f_S - 2f_N f_S), \qquad (18)$$

together with DOS functions $f_N = f(\epsilon + eV_J, T_0)$ and $f_S = f(\epsilon, T_B)$.

At low temperatures, simple approximations can be used for the tunnel current and cross-correlated noises in Eqs.(18). These are expressed as $\langle\delta I_J^2\rangle \approx 2eI_J$ and $\langle\delta I_J P_J\rangle \approx -2eP_J$[13]. In contrast, the analytical expression for tunnel heat noise at optimal bias consists of three key terms:

$$\langle\delta P_J^2\rangle \approx 4\sqrt{2\pi}\frac{\Delta_0^3}{e^2 R_T}\left(\frac{k_B T_S}{\Delta_0}\right)^{\frac{1}{2}}e^{-\Delta_0/k_B T_S}$$
$$+ 2.05\frac{\Delta_0^3}{e^2 R_T}\left(\frac{k_B T_0}{\Delta_0}\right)^{\frac{5}{2}} + \frac{2}{3}\frac{(eV_{\text{opt}})^3}{e^2 R_T}\Gamma. \qquad (19)$$

Here, the first two terms represent the thermal fluctuations resulting from the finite temperatures of the superconductor, and normal metal absorber, while the third term accounts for noise from the subgap tunneling current, characterized by Γ.

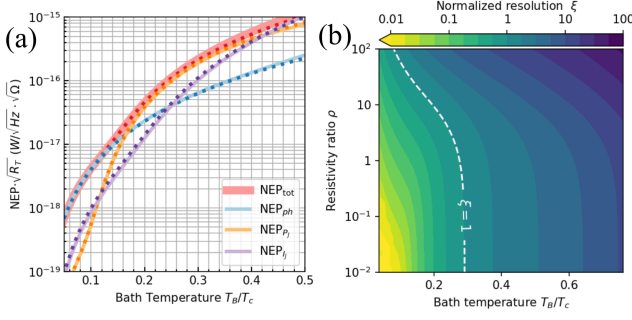Substituting Eq.(16) with the analytical expressions from Eqs.(5),(6),(12), and (19) and performing algebraic

FIG. 4. (a) Numerically calculated total NEP and its decompositions of various contributions in Eq.(15) (solid colored line), scaled as NEP $\cdot \sqrt{R_T}$, as a function of T_B/T_c for an ideal detector with $\rho = 1$. They are also compared with the analytical approximations (dotted colored lines). (b) Numerically calculated normalized resolution ξ as a function of T_B/T_c and ρ.

simplifications, the total NEP of the detector at V_{opt} becomes:

$$
\begin{aligned}
\mathrm{NEP}_{\mathrm{tot}}^2 \approx {}& 4k_B T_B^2 G_{\mathrm{th}}(1-\eta)^2 \left[0.48 \frac{1-\kappa}{(1-\eta)^5} \right. \\
& + 2.8 \frac{\kappa \beta_B^2}{(1-\eta)^{\frac{5}{2}}} e^{-\beta_B} + 0.19\kappa\Gamma\beta_N^{\frac{5}{2}} + 0.58\kappa \\
& + 3.7 \frac{1}{\kappa\alpha_T^2}(1+\omega^2\tau_{\mathrm{th}}^2) - 2.46\frac{1}{\alpha_T} \\
& \left. + 2.1 \frac{R_T}{\alpha_T^2\Delta_0}\sqrt{\frac{\beta_B}{1-\eta}}(1+\omega^2\tau_{\mathrm{th}}^2)\langle\delta I_{\mathrm{Amp}}^2\rangle \right],
\end{aligned}
\tag{20}
$$

where $\kappa = G_c/G_{\mathrm{th}} = 1/[1 + 0.56\rho(T_0/T_c)^{2.5}]$, $\beta_B = \Delta_0/k_B T_B$ and $\beta_N = eV_{\mathrm{opt}}/k_B T_0$ are introduced for clarity. The first row represents the contribution from TFN, which vanishes if the thermal conductance from phonons, G_{ph}, is much smaller than that from the junction heat current, meaning $\kappa = 1$. The second row captures the noise power from the junction heat current, with the first term rapidly diminishing at $T_B < 0.2T_c$. The third row represents the noise generated by the electrical current, which includes a cutoff frequency limiting the high-frequency responsivity, as well as a negative term reflecting the noise correlation between the electrical and heat current in the junction. Finally, the last term accounts for the readout noise, which will be neglect for an ideal detector.

Figure 4(a) illustrates the NEP of an ideal detector with $\rho = 1$, operating at its optimal bias point[36]. The red solid line represents the numerically calculated total NEP, which decreases with bath temperature and is inversely proportional to $\sqrt{R_T}$. This behavior indicates that more resistive junctions generate less noise, a trend that contrasts with the detector's thermal time constant τ_{th}, which increases with R_T. The red dotted line corresponds to the approximate expression from Eq.(20), showing excellent agreement with the numerical results

up to $0.5T_c$. This consistency provides valuable insight into the noise characteristics of the detector.

To further understand the noise behavior, panel (a) also breaks down the contributions from individual noise components, computed using both numerical methods (solid colored lines) and analytical approximations (dotted colored lines). At higher temperature $T_B/T_c > 0.44$, the thermal conductance ratio κ becomes much smaller than 1, making the electric current noise, $\mathrm{NEP}_{I_J} = 2\langle\delta I_J^2\rangle/|S_I(\omega)|^2$, the dominant source. As the temperature decreases to intermediate level, κ increases, leading to a more significant contribution from the junction's heat current noise, $\mathrm{NEP}_{P_J} = 2\langle\delta P_J^2\rangle$. In the low-temperature limit $T_B/T_c < 0.16$, the phonon noise, $\mathrm{NEP}_{P_{\mathrm{ph}}} = \langle\delta P_{\mathrm{TFN}}^2\rangle$, begin to dominate. This aligns with Eq.(20), as the cooling factor η in an ideal detector approaches 1, amplifying the first term in the noise expression.

This analysis also reveals a fundamental low-temperature limit for the NEP in an ideal detector, where heat dissipation occurs exclusively through the junction's heat current ($\kappa = 1$). In this regime, the NEP approaches $\mathrm{NEP}_{\mathrm{tot}}(0) = 2.7(1-\eta)\sqrt{k_B T_B^2 G_{\mathrm{th}}}$, setting a noise floor achievable by the detector.

The FWHM energy resolution ΔE can be obtained straightwardly using Eq.(14). At the optimal bias, it reads as:

$$
\Delta E = \xi \times 2.35\sqrt{k_B T_B^2 C_{\mathrm{th}}} \tag{21}
$$

where ξ is approximated by:

$$
\begin{aligned}
\xi = {}& 2\frac{1-\eta}{\sqrt{\alpha_T}}\left[1.8\frac{1-\kappa}{\kappa(1-\eta)^5} \right. \\
& + \left(0.7\Gamma + 10.5\beta_B^{-\frac{1}{2}}e^{-\beta_B}\right)\beta_N^{\frac{5}{2}} + 2.1 \\
& \left. + \frac{1}{\kappa^2\alpha_T^2}\left(13.7 - 9.1\kappa\alpha_T\right) \right]^{\frac{1}{4}}
\end{aligned}
\tag{22}
$$

Figure 4(b) presents the numerically calculated normalized resolution ξ as a function of normalized bath temperature (T_B/T_c) and resistivity ratio for an ideal detector biased at V_{opt}. ξ decreases with lower T_B and smaller ρ, eventually approaching saturation when ρ is small. Notably, ξ can drop below 1, indicating that the energy resolution surpasses the intrinsic TFN limit. The threshold for $\xi < 1$ is depicted by the white dashed line in the figure and occurs at approximately $0.3T_c$ for $\rho < 1$.

At low temperatures, a fundamental resolution limit can be derived under the same assumptions used for the NEP by setting $\kappa = 1$. This yields a resolution of $\Delta E \approx 3.3(1-\eta) \times \Delta E_{\mathrm{intrinsic}}$. A similar factor was proposed by Nahum and Martinis[18, 19], but their model did not account for the cooling effect ($\eta = 0$). This result suggests that achieving a cooling factor $\eta > 70\%$ enables cold-electron microcalorimeters to surpass the intrinsic TFN limit.

Superconducting gap Δ_0	0.2 meV
Normal state resistance R_T	2.5 Ω
Dynes parameter Γ	10^{-3}
Heat return coefficient β	0
Interfacial thermal resistance a_{eITR}	0.1 K^4/nW
Absorber Sommerfeld coefficient γ	2 pJ/K^2
Input coil inductance L	1.8 μH
SQUID readout noise $\langle \delta I^2_{\mathrm{Amp}} \rangle$	60 fA/$\sqrt{Hz}$

TABLE I. Key parameters of the proposed device.

For comparison, the optimal resolution for an ideal TES detector is given by $\xi = 2.4/\sqrt{\alpha_{\mathrm{TES}}}$[1, 7], where α_{TES} can exceed 100. To match the best TES performance, NIS junctions would require an on-chip cooling factor of approximately 90%. Encouragingly, recent experiments have shown that NIS tunnel junctions can achieve cooling factors greater than 80% at bath temperatures of 200-300 mK[17], and cooling of bulk silicon plates with a factor of 40% has also been demonstrated[8].

V. NON-IDEAL DEVICE

In previous sections, the general theory for a phonon-blocked cold-electron microcalorimeter was established, and numerical results were presented in scaled units for an ideal device. In this section, the focus moves to estimating the performance of a practical device using a set of realistic parameters. This approach provides insight into the expected performance of a real-world detector and serves as a baseline to showcase the impact of non-ideal parameters on detector performance.

The key parameters of the device investigated in this section are summarized in Table I.

The tunnel junction is modeled with a superconducting gap $\Delta_0 = 0.2$ meV, *e.g.* aluminum, and an area of 80 μm^2. Each junction has a normal state resistance of $R_T = 2.5$ Ω by assuming a sheet resistance of 200 $\Omega \, \mu m^2$. Two phenomenological parameters, the Dynes parameter Γ and the heat return coefficient β, are set to 10^{-3} and 0[21, 37], respectively.

The phonon channel is assumed to be limited by interfacial thermal resistance, and the area resistance is set to 15.4 K$^4\mu m^2$/nW[22], leading to an effective interfacial thermal resistance of $a_{\mathrm{eITR}} = 0.1$ K^4/nW. The heat capacity of the absorber is assumed to be dominated by the electron system within the temperature range of interest, with $\gamma = 2$ pJ/K^2, resulting in a temperature increase of less than 5% at 0.1 K for an absorbed 6 keV photon.

Finally, the SQUID readout amplifies the current signal. The values for the input coil inductance and amplifier current noise are based on commercially available products[38], which give a negligible contribution to the detector noise.

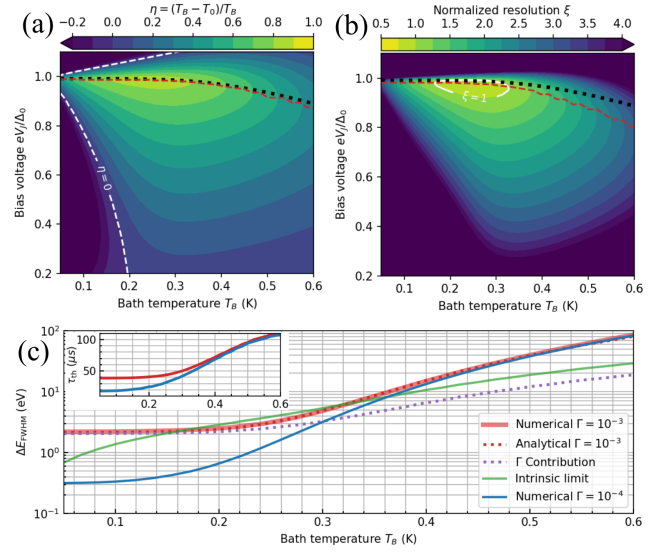Figure 5 provides a detailed look at the numerically

FIG. 5. (a) and (b) cooling factor η and normalized resolution ξ as a function of bath temperature and bias voltage of a practical detector. (c) Comparison of the energy resolution results as a function of bath temperature.

computed performance of the practical microcalorimeter, showcasing how realistic device parameters affect both cooling efficiency and energy resolution.

In panel (a), the cooling factor η is plotted as a function of bath temperature T_B and bias voltage V_J. The red dashed line indicates the bias voltage that maximizes cooling, closely following the approximate optimal bias V_{opt} (black dotted line). Moving away from this optimal point, cooling effectiveness diminishes, and at certain voltages, even switches to heating, with the boundary shown by the white dashed line where $\eta = 0$. Unlike an ideal detector, where η increases with lowering temperature, the practical device achieves a maximum of 85% around 0.25 K, close to that reported in experiment[17]. This saturation is attributed to subgap tunneling effects, characterized by $\Gamma = 10^{-3}$, which dominates the detector performance at low temperatures. Subgap tunneling smears the singularity of superconducting density of states by allowing states to appear within the gap[39], reducing the efficiency of hot electron filtering and causing excess Joule heating. This effect introduces additional voltage-dependent heating as shown in Eq.(6), independent of bath temperature, which reduces cooling efficiency at lower temperatures.

Panel (b) presents the normalized energy resolution ξ as a function of temperature and bias voltage. The red dashed line marks the voltage that minimizes ξ, located slightly below V_{opt}. This shift occurs because subgap tunneling introduces an additional resolution penalty that depends on V_J, slightly lowering the optimal bias for minimizing ξ. Notably, a region where $\xi < 1$ appears around a bath temperature of 0.25 K, enclosed by the white solid line, indicating that the device can achieve
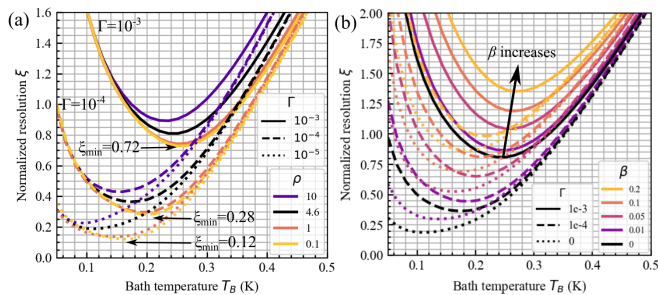
FIG. 6. (a) Normalized resolution ξ as a function of bath temperature for different values of the Dynes parameter Γ, indicated by solid, dashed and dotted lines, and for different ρ, indicated by different colors. (b) ξ versus heat backflow coefficient β (colored) at varying values of Γ.

an energy resolution surpassing the intrinsic TFN limit, with a minimum ξ of 0.8.

Finally, panel (c) displays the numerically calculated energy resolution at the optimal bias as a red solid line, with the red dotted line showing the analytical approximation presented in Eq.(22), which matches well with the numerical results. This alignment provides a basis for understanding how each parameter influences the energy resolution. At bath temperatures below 0.15 K, the energy resolution saturates around $\Delta E \approx 2$ eV, largely due to noise from subgap tunneling, depicted by the violet dotted line. This is also confirmed by comparing it to the numerical result of a detector with a same ρ but lower $\Gamma = 10^{-4}$ (blue solid line), revealing a degradation in resolution starting from $T_B = 0.4$ K. Nevertheless, the device still achieves a resolution below the intrinsic TFN limit (green solid line) within the temperature range of 0.15 K to 0.3 K, illustrating its robustness despite non-idealities. Additionally, the inset in panel (c) highlights a fast thermal response, with a time constant of approximately 50 μs, underscoring that the detector is also suitable for applications requiring high bandwidth.

As demonstrated in the preceding analysis, subgap tunneling substantially reduces detector performance. To optimize the device, reducing this leakage is essential. In practical applications, the Dynes parameter Γ depends on the transparency of the junction barrier[40]. For aluminum-based junctions, typical values for Γ are around 10^{-4}, though values as low as 10^{-7} have been achieved[41]. Additionally, recent studies suggest that hybrid superconducting/ferromagnetic structures may effectively suppress Andreev current, lowering Γ and thus enhancing junction cooling[17, 42, 43].

Figure 6(a) illustrates how reducing Γ improves ξ by comparing three values of Γ with all other parameters held constant, as shown with the black lines. Lowering Γ from 10^{-3} (black solid line) to 10^{-4} (black dashed line) reduces the minimum ξ from 0.8 to 0.36, achieving an energy resolution $\Delta E_{\mathrm{FWHM}} = 0.5$ eV at a bath temperature of 170 mK. This strong improvement in energy resolution can be seen more clearly in Fig. 5(c) from the blue solid

line. It saturates at a lower temperature $T_B < 0.1$ K with a much lower resolution about 0.3 eV, significantly lower than the reported TES detectors. In addition, it also further improves the speed of the detector, reaching 20 μs at low temperature. Further decreasing of the subgap leakage (i.e., $\Gamma = 10^{-5}$ depicted as black dotted line) optimizes ξ further and allows for operation at lower optimal bath temperatures.

Beyond reducing Γ, performance can be further enhanced by optimizing the resistivity ratio ρ through engineering the junction interface and barrier[44]. For the device demonstrated in Figure 6 (a), the decrease in ρ generally improves ξ, as shown by the colored lines: at $\rho = 0.1$, ξ reaches the minima of 0.72 ($\Gamma = 10^{-3}$, solid yellow line) and 0.28 ($\Gamma = 10^{-4}$, dashed yellow line), approaching the theoretical limits for ideal TES detectors. Further reduction below $\rho = 0.1$ yields diminishing returns, consistent with the saturation trends in Figure 4(b).

Lastly, we briefly address heat backflow from the hot quasiparticles in the superconductor electrode to the normal metal, characterized by the phenomenological parameter β. A nonzero β reduces the net cooling power proportionally, as the backflow heat scales with both junction cooling and Joule heating $[2\beta(P_J + I_J V_J)]$. Figure 6(b) illustrates how increasing β degrades the normalized energy resolution. For instance, with $\Gamma = 10^{-3}$ (solid colored lines), values of $\beta > 0.05$ push the resolution above the intrinsic TFN limit ($\xi > 1$). For lower values of Γ, the tolerance to backflow increases; for example, at $\Gamma = 10^{-4}$ (dashed colored lines), β must exceed 0.2 to compromise the resolution above the TFN limit. This again emphasizes the importance of optimizing subgap tunneling. In practice, backflow can be mitigated by incorporating quasiparticle traps, such as an additional normal metal layer on the superconductor electrode [45–47].

VI. CONCLUSIONS

In this work, we have presented a general theory of a cold-electron microcalorimeter based on phonon-blocked tunnel junctions, demonstrating its potential as highly sensitive and fast cryogenic detector. A key contribution of this study is the derivation of approximate analytical expressions for critical performance metrics, such as responsivity, noise equivalent power and energy resolution. These expressions not only provide insight into the fundamental performance of an ideal detector, but also serve as valuable tools for guiding the optimization of non-ideal devices.

Our analysis reveals that, under ideal conditions, the energy resolution of the phonon-blocked junction microcalorimeter can achieve approximately $3.3(1 - \eta)\Delta E_{\mathrm{intrinsic}}$, rivaling the theoretical limits of TES detectors. Notably, we identified that the detector's key performance metrics, such as cooling factor η, responsiv-

ity $S_I(0)$, and normalized energy resolution ξ, are largely independent of the junction area. Instead, they are governed by ρ, a dimensionless parameter that characterizes the ratio between the normal-state electrical resistance R_T and the interfacial thermal resistance a_{eITR}. This independence, coupled with the finding that the thermal time constant τ_{th} is proportional to $R_T\sqrt{T_0}$, underscores the potential for achieving both high resolution and fast thermal response by employing large-area junctions at low temperatures.

The study also highlights the challenges posed by nonidealities, particularly subgap tunneling, which can significantly degrade the performance. However, our practical device example demonstrates that, as already demonstrated with experimentally achieved parameters, the detector can achieve energy resolutions the intrinsic thermal fluctuation noise limit ($\xi < 1$). With further optimization of subgap tunneling, an area where recent experiments using hybrid superconducting/ferromagnetic structures have already shown promising results, phonon-blocked junction microcalorimeters have the potential to outperform the theoretical performance of TES detectors.

In conclusion, the phonon-blocked junction microcalorimeter represents a promising alternative to TES technology, offering exceptional energy resolution and fast thermal response. Its ability to achieve on-chip cooling minimizes the need for complex cryogenic setups, making it ideal for applications requiring precise energy detection at high bandwidth. With further advancements in reducing subgap tunneling and optimizing interface properties, such detector has the potential to set new benchmark in cryogenic microcalorimetry and expand the possibilities for future scientific and technological advancements.

[1] C. Enss, ed., *Cryogenic Particle Detection* (Springer, Berlin, Heidelberg, 2005).

[2] C. W. Fabjan and H. Schopper, eds., *Particle Physics Reference Library: Volume 2: Detectors for Particles and Radiation* (Springer, Cham, 2020).

[3] L. D. Landau and E. M. Lifshitz, *Statistical physics*, 3rd ed. (Elsevier, Amsterdam Heidelberg, 1980).

[4] T. C. P. Chui, D. R. Swanson, M. J. Adriaans, J. A. Nissen, and J. A. Lipa, Temperature fluctuations in the canonical ensemble, Phys. Rev. Lett. **69**, 3005 (1992).

[5] J. N. Ullom, J. A. Beall, W. B. Doriese, W. D. Duncan, L. Ferreira, G. C. Hilton, K. D. Irwin, C. D. Reintsema, and L. R. Vale, Optimized transition-edge x-ray microcalorimeter with 2.4 eV energy resolution at 5.9 keV, Appl. Phys. Lett. **87**, 1 (2005).

[6] J. N. Ullom and D. A. Bennett, Review of superconducting transition-edge sensors for x-ray and gamma-ray spectroscopy, Supercond. Sci. Technol. **28**, 084003 (2015).

[7] K. D. Irwin, An application of electrothermal feedback for high resolution cryogenic particle detection, Appl. Phys. Lett. **66**, 1998 (1995).

[8] E. Mykkänen, J. S. Lehtinen, L. Grönberg, A. Shchepetov, A. V. Timofeev, D. Gunnarsson, A. Kemppinen, A. J. Manninen, and M. Prunnila, Thermionic junction devices utilizing phonon blocking, Sci. Adv. **6**, eaax9191 (2020).

[9] F. Giazotto, T. T. Heikkilä, A. Luukanen, A. M. Savin, and J. P. Pekola, Opportunities for mesoscopics in thermometry and refrigeration: Physics and applications, Rev. Mod. Phys. **78**, 217 (2006).

[10] J. T. Muhonen, M. Meschke, and J. P. Pekola, Micrometre-scale refrigerators, Rep. Prog. Phys **75**, 046501 (2012).

[11] M. Nahum and J. M. Martinis, Ultrasensitive-hot-electron microbolometer, Appl. Phys. Lett. **63**, 3075 (1993).

[12] L. S. Kuzmin, On the concept of a hot-electron microbolometer with capacitive coupling to the antenna, Phys. Rev. B Condens. Matter **284–288**, 2129 (2000).

[13] D. Golubev and L. Kuzmin, Nonequilibrium theory of a hot-electron bolometer with normal metal-insulator-superconductor tunnel junction, J. Appl. Phys. **89**, 6464 (2001).

[14] D. V. Anghel and J. P. Pekola, Noise in refrigerating tunnel junctions and in microbolometers, J. Low Temp. Phys. **123**, 197 (2000).

[15] D. V. Anghel, A. Luukanen, and J. P. Pekola, Performance of cryogenic microbolometers and calorimeters with on-chip coolers, Appl. Phys. Lett. **78**, 556 (2001).

[16] L. S. Kuzmin, A. L. Pankratov, A. V. Gordeeva, V. O. Zbrozhek, V. A. Shamporov, L. S. Revin, A. V. Blagodatkin, S. Masi, and P. De Bernardis, Photon-noise-limited cold-electron bolometer based on strong electron self-cooling for high-performance cosmology missions, Commun. Phys. **2**, 104 (2019).

[17] A. V. Gordeeva, A. L. Pankratov, N. G. Pugach, A. S. Vasenko, V. O. Zbrozhek, A. V. Blagodatkin, D. A. Pimanov, and L. S. Kuzmin, Record electron self-cooling in cold-electron bolometers with a hybrid superconductor-ferromagnetic nanoabsorber and traps, Sci. Rep. **10**, 21961 (2020).

[18] M. Nahum, J. M. Martinis, and S. Castles, Hot-electron microcalorimeters for x-ray and phonon detection, J. Low Temp. Phys. **93**, 733 (1993).

[19] M. Nahum and J. M. Martinis, Hot-electron microcalorimeters as high-resolution x-ray detectors, Appl. Phys. Lett. **66**, 1478 (1995).

[20] J. N. Ullom, Physics and applications of NIS junctions, AIP conf. proc. **605**, 135 (2003).

[21] A. Kemppinen, A. Ronzani, E. Mykkänen, J. Hätinen, J. S. Lehtinen, and M. Prunnila, Cascaded superconducting junction refrigerators: Optimization and performance limits, Appl. Phys. Lett. **119**, 052603 (2021).

[22] J. Hätinen, E. Mykkänen, K. Viisanen, A. Ronzani, A. Kemppinen, L. Lehtisyrjä, J. S. Lehtinen, and M. Prunnila, Thermal resistance in superconducting flip-chip assemblies, Appl. Phys. Lett. **123**, 152202 (2023).

[23] E. T. Swartz and R. O. Pohl, Thermal boundary resistance, Rev. Mod. Phys. **61**, 605 (1989), 1407.6410.

[24] P. A. Fisher, J. N. Ullom, and M. Nahum, High-power on-chip microrefrigerator based on a normal-metal/insulator/superconductor tunnel junction, Appl. Phys. Lett. **74**, 2705 (1999).

[25] For typical Au absorbers (thickness$\approx \mu$m, area$\geq 50 \times 50\,\mu$m^2), the sheet resistance $10^{-5}\,m\Omega$·cm yields a total resistance $< 10^{-8}\Omega$. Resulting Joule heating I^2R is orders below cooling power and other thermal terms, justifying its neglect.

[26] J. Jochum, C. Mears, S. Golwala, B. Sadoulet, J. P. Castle, M. F. Cunningham, O. B. Drury, M. Frank, S. E. Labov, F. P. Lipschultz, H. Netel, and B. Neuhauser, Modeling the power flow in normal conductor-insulator-superconductor junctions, J. Appl. Phys. **83**, 3217 (1998).

[27] S. Chaudhuri and I. J. Maasilta, Cooling, conductance, and thermometric performance of nonideal normal metal-superconductor tunnel junction pairs, Phys. Rev. B **85**, 014519 (2012), 1112.0197.

[28] R. C. Dynes, V. Narayanamurti, and J. P. Garno, Direct Measurement of Quasiparticle-Lifetime Broadening in a Strong-Coupled Superconductor, Phys. Rev. Lett. **41**, 1509 (1978).

[29] S. H. Moseley, J. C. Mather, and D. McCammon, Thermal detectors as x-ray spectrometers, J. Appl. Phys. **56**, 1257 (1984).

[30] b_0 is derived from time domain balance equations. It reflects the feedback effect from the change of voltage, $b_0 = 2\partial P_J \partial I_J / \partial^2 V V_0$ if $\beta = 0$. The constant current thermal time constant is modified by this factor as well as the constant current loop gain $\mathcal{L}_0$ reads as $\tau_I := \tau_{th}/(1 - b_0 \mathcal{L}_0)$.

[31] S. J. Lee, J. S. Adams, S. R. Bandler, J. A. Chervenak, M. E. Eckart, F. M. Finkbeiner, R. L. Kelley, C. A. Kilbourne, F. S. Porter, J. E. Sadleir, S. J. Smith, and E. J. Wassell, Fine pitch transition-edge sensor X-ray microcalorimeters with sub-eV energy resolution at 1.5 keV, Appl. Phys. Lett. **107**, 223503 (2015).

[32] A. R. Miniussi, J. S. Adams, S. R. Bandler, J. A. Chervenak, A. M. Datesman, M. E. Eckart, A. J. Ewin, F. M. Finkbeiner, R. L. Kelley, C. A. Kilbourne, F. S. Porter, J. E. Sadleir, K. Sakai, S. J. Smith, N. A. Wakeham, E. J. Wassell, and W. Yoon, Performance of an X-ray Microcalorimeter with a 240 Mm Absorber and a 50 Mm TES Bilayer, J. Low Temp. Phys. **193**, 337 (2018).

[33] S. R. Bandler, J. A. Chervenak, A. M. Datesman, A. M. Devasia, M. DiPirro, K. Sakai, S. J. Smith, T. R. Stevenson, W. Yoon, D. Bennett, B. Mates, D. Swetz, J. N. Ullom, K. D. Irwin, and M. E. Eckart, Lynx x-ray microcalorimeter, J. Astron. Telesc. **5**, 1 (2019).

[34] K. Sakai, S. V. Hull, J. S. Adams, S. R. Bandler, S. Beaumont, R. B. Borrelli, J. A. Chervenak, R. S. Cumbee, F. M. Finkbeiner, J. Y. Ha, R. L. Kelley, C. A. Kilbourne, M. A. Leutenegger, J. N. Mateo, H. Muramatsu, F. S. Porter, S. J. Smith, N. A. Wakeham, E. J. Wassell, S. H. Yoon, and M. E. Eckart, Demonstration of a Full-Scale Brassboard TES Microcalorimeter Array for the *Athena* X-IFU, IEEE Trans. Appl. Supercond. **33**, 1 (2023).

[35] Y. M. Blanter and M. B uttiker, Shot noise in mesoscopic conductors, Phys. Rep. **336**, 1 (2000).

[36] There is a discrepancy between the approximate optimal voltage $V_{\rm opt}$ and the voltage at the numerical minimum. This difference occurs because the NEP contribution from the junction heat current, $\langle \delta P_J^2 \rangle$, is not influenced by the detector's sensitivity. It approaches zero as the bias voltage decreases, causing the NEP to reach its minimum at a voltage slightly lower than $V_{\rm opt}$. Nevertheless, discussions on the detector noise will still be carried out at the optimal bias, as the optimal energy resolution occurs at $V_{\rm opt}$. This is because the reduction in noise from the heat current is offset by the increase in the thermal time constant, which will be demonstrated later.

[37] D. Gunnarsson, J. S. Richardson-Bullock, M. J. Prest, H. Q. Nguyen, A. V. Timofeev, V. A. Shah, T. E. Whall, E. H. C. Parker, D. R. Leadley, M. Myronov, and M. Prunnila, Interfacial Engineering of Semiconductor–Superconductor Junctions for High Performance Micro-Coolers, Sci. Rep. **5**, 17398 (2015).

[38] E. L. Wolf, G. Arnold, M. Gurvitch, and J. Zasadzinski, eds., *Josephson Junctions: History, Devices, and Applications* (Pan Stanford Publishing, Singapore, 2017).

[39] J. P. Pekola, T. T. Heikkilä, A. M. Savin, J. T. Flyktman, F. Giazotto, and F. W. J. Hekking, Limitations in Cooling Electrons using Normal-Metal-Superconductor Tunnel Junctions, Phys. Rev. Lett. **92**, 056804 (2004).

[40] A. S. Vasenko, E. V. Bezuglyi, H. Courtois, and F. W. J. Hekking, Electron cooling by diffusive normal metal–superconductor tunnel junctions, Phys. Rev. B **81**, 094513 (2010).

[41] J. P. Pekola, V. F. Maisi, S. Kafanov, N. Chekurov, A. Kemppinen, Yu. A. Pashkin, O.-P. Saira, M. Möttönen, and J. S. Tsai, Environment-Assisted Tunneling as an Origin of the Dynes Density of States, Phys. Rev. Lett. **105**, 026803 (2010).

[42] F. Giazotto, F. Taddei, R. Fazio, and F. Beltram, Ultra-efficient cooling in ferromagnet–superconductor microrefrigerators, Appl. Phys. Lett. **80**, 3784 (2002).

[43] A. Ozaeta, A. S. Vasenko, F. W. J. Hekking, and F. S. Bergeret, Electron cooling in diffusive normal metal–superconductor tunnel junctions with a spin-valve ferromagnetic interlayer, Phys. Rev. B **85**, 174518 (2012).

[44] J. C. Duda and P. E. Hopkins, Systematically controlling Kapitza conductance via chemical etching, Appl. Phys. Lett. **100**, 111602 (2012).

[45] J. P. Pekola, D. V. Anghel, T. I. Suppula, J. K. Suoknuuti, A. J. Manninen, and M. Manninen, Trapping of quasiparticles of a nonequilibrium superconductor, Appl. Phys. Lett. **76**, 2782 (2000).

[46] G. C. O'Neil, P. J. Lowell, J. M. Underwood, and J. N. Ullom, Measurement and modeling of a large-area normal-metal/insulator/superconductor refrigerator with improved cooling, Phys. Rev. B **85**, 134504 (2012).

[47] H. Q. Nguyen, T. Aref, V. J. Kauppila, M. Meschke, C. B. Winkelmann, H. Courtois, and J. P. Pekola, Trapping hot quasi-particles in a high-power superconducting

electronic cooler, New J. Phys. **15**, 085013 (2013).